JOURNAL OF MATERIALS SCIENCE 24 (1989) 863–872

Analytical transmission electron microscopy of La_2O_3-doped Y_2O_3

S. F. HORVATH, M. P. HARMER, D. B. WILLIAMS, M. R. NOTIS
Department of Materials Science and Engineering, Lehigh University, Bethlehem, Pennsylvania 18015, USA

Analytical electron microscopy has been used to study the precipitation reactions in sintered samples of 9 mol % La_2O_3–Y_2O_3 samples upquenched from the single phase cubic region into the cubic and hexagonal phase field. Samples annealed just inside the two-phase cubic–cubic and hexagonal solvus exhibited predominantly grain boundary precipitation. Small La_2O_3 rich second phases formed within the first ten minutes and developed into strained, facetted precipitates after 300 min. Intergranular and intragranular precipitation occurred in samples annealed further into the two-phase field. Strained, lathlike La_2O_3-rich monoclinic precipitates, exhibiting a preferrred orientation in the matrix, appeared as the dominant morphology for long times at temperature. Chemical microanalyses of the strained structures obtained in samples annealed for 300 min revealed La_2O_3 matrix concentrations in agreement with phase diagram predictions. However, the La_2O_3 concentrations in the second-phase precipitates were found to be far in excess of the cubic and hexagonal–hexagonal solvus. This discrepancy is believed to arise from a re-equilibration of the second phase in the cubic and monoclinic phase field during quenching.

1. Introduction

Current investigations on yttrium oxide, the most abundant of the rare earth oxides, have focused on the unique optical properties of this ceramic [1–3]. Y_2O_3 exhibits great potential as an optical material due to its isotropic (cubic) structure, chemical stability, and excellent light transmittance capabilities which extend further into the infrared than most other oxides. As a result, this oxide is becoming competitive with other infrared materials such as Al_2O_3.

Over the years, sintering methods have been sought for the development of fully dense, highly transparent Y_2O_3. Rhodes [1] has developed a transient second-phase sintering technique based upon the Y_2O_3–La_2O_3 binary that results in transparent, stoichiometric, polycrystalline Y_2O_3 solid solution material. The use of La_2O_3 as a sintering aid avoids the toxicity problems and chemical instability problems encountered by other investigators in previous sintering attempts using BeO and ThO_2 as sintering additives [4]. Rhodes' technique consists of sintering Y_2O_3 doped with 8–14 mol % La_2O_3 in the two-phase cubic and hexagonal field very close to the cubic and cubic–hexagonal solvus (see Fig. 1). The hexagonal phase precipitates on the grain boundaries and pins their motion, preventing pore-boundary breakaway and thus helps facilitate pore annihilation by diffusion along the boundary. A lower temperature anneal in the single-phase cubic region dissolves the second phase yielding a fully dense highly transparent homogeneous polycrystalline yttrium oxide ceramic.

Currently, interest has developed in the nature of the phase transitions involved in the Y_2O_3–La_2O_3 binary. Preliminary X-ray investigations by Wei *et al.* [5] on 8–14 mol % lanthana-doped Y_2O_3 samples, quenched from the two-phase cubic and hexagonal phase field, revealed that the hexagonal phase rapidly transforms to the lower symmetry monoclinic form on cooling. Electron microscopy revealed that twinning and slip accompany the transformation yielding microstructures very similar to those obtained for the tetragonal to monoclinic transformation in ZrO_2. Unlike the zirconia system and even other rare earth oxide systems, the precipitation events in the Y_2O_3–La_2O_3 binary have not been extensively researched. Studies of other rare earth systems have shown the hexagonal and monoclinic structures to be closely related and that the monoclinic cell can be derived from the former by slight shifts of the hexagonal structure in a diffusionless, displacive manner [6–14]. However, most of the major work on yttria–lanthana has focused on the phase diagram determination by high temperature X-ray diffraction. Only limited electron microscopy studies have been performed on this system [15].

The yttria-rich portion of the diagram is shown in Fig. 1. It consists primarily of a two-phase cubic and hexagonal field above a single phase cubic region for lanthana concentrations up to approximately 20 mol %. A eutectoid reaction occurs near 1850° C for 30 mol % lanthana concentrations where the hexagonal phase transforms to the cubic and monoclinic structures. This diagram, taken from high temperature X-ray data by Mizuno *et al.* [16] and Coutures and Foex [17] exhibits some uncertainty in the limits of the two-phase cubic and monoclinic field

0022–2461/89 $03.00 + .12

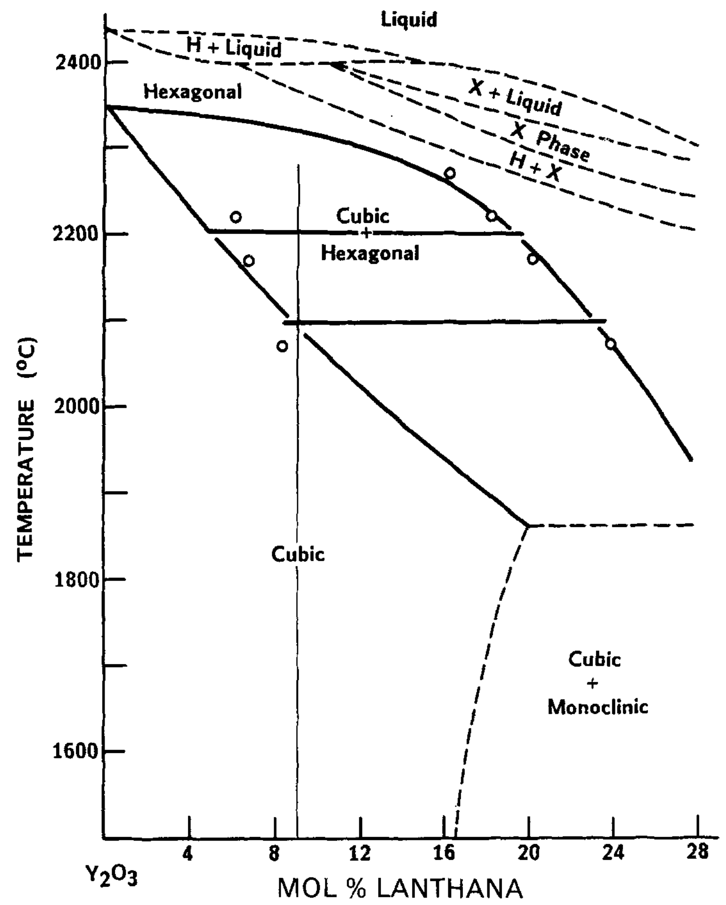

Figure 1 The high temperature portion of the Y_2O_3-rich region of the Y_2O_3–La_2O_3 phase diagram (after Mizuno [16] and Coutures and Foex [17]). Vertical line depicts the Y_2O_3–La_2O_3 concentration used in the present study and the two tie lines show the expected concentrations of the two phases at 2100 and 2200° C.

as well as the eutectoid temperature although the cubic and monoclinic field appears well defined. Rhodes' [5] findings of cubic and monoclinic structures in 8–14 mol % lanthana samples quenched from the cubic and hexagonal region indicate that the limit of the lanthana concentration in yttria below 1850° C may be less than that shown on the diagram. The circles in the cubic and hexagonal region are data points obtained by Rhodes using microprobe analysis on large individual abnormal grains of 12–14 mol % La_2O_3 samples sintered at 2070 and 2270° C and quenched to 1400° C in 1 min. These results show excellent agreement with the cubic–cubic and hexagonal solvus but exhibit some slight anomalies when compared with the published cubic and cubic–hexagonal solvus boundary.

The objective of the present study is to apply the technique of analytical transmission electron microscopy (TEM) to study the precipitation phenomena in the yttria-rich portion of the yttria–lanthana binary. In particular, the nature of the precipitation of the hexagonal phase in the cubic matrix and its behaviour upon quenching will be addressed. Major emphasis is placed on analytical results obtained from 9 mol % La_2O_3–Y_2O_3 samples annealed for long times in the two-phase field. These results will be compared with the present phase diagram predictions.

2. Experimental details

Nine mol % La_2O_3–Y_2O_3 powder mixtures were prepared by an oxalate coprecipitation technique. The cold pressed pellets were sintered in the single-phase cubic region at 1950° C for 3 h. They were then upquenched into the two-phase field and held at 2100° C for various times ranging from 1 to 300 minutes. The same procedure was followed for a second set of samples which were held at 2200° C for the same amounts of time. All treatments were performed in a tungsten mesh resistance heated furnace using a wet hydrogen atmosphere (23° C dew point) and were terminated with quenches to room temperature. The quenching procedure involved cutting the power to the furnace and allowing the temperature to fall at an approximate rate of 350 to 400° C min^{-1}.

Thin foils were prepared by slicing cross-sections of the sintered pellet and grinding them with 600 grit and 1200 grit silicon carbide powder to less than 100 μm before polishing both sides with 6 μm diamond paste. Polished foils were then mounted between two rhodium plated copper grids and ion beam thinned at 6 kV. All TEM analyses were performed at 120 kV on a Phillips 400T equipped with an EDAX energy dispersive X-ray spectrometer.

A homogeneous Y_2O_3–9 mol % La_2O_3 sample was prepared by GTE laboratories as a standard for the *k*-factor determination in this system. The sample was sintered at 2150° C for 90 min, cooled to room temperature, and then annealed at 1950° C for 6 h for homogenization. Wet chemistry analysis by the inductively coupled plasma (ICP) technique was performed to assess the concentrations of yttrium and lanthanum metal. Microprobe analyses on the bulk using the sample as its own standard and measuring oxygen by difference confirmed the homogeneity of the sample within the limits of resolution of the instrument. *k*-factor measurements were performed on thin foils in both TEM and STEM modes at 120 kV. A window of approximately 1.2 times the full width half maximum

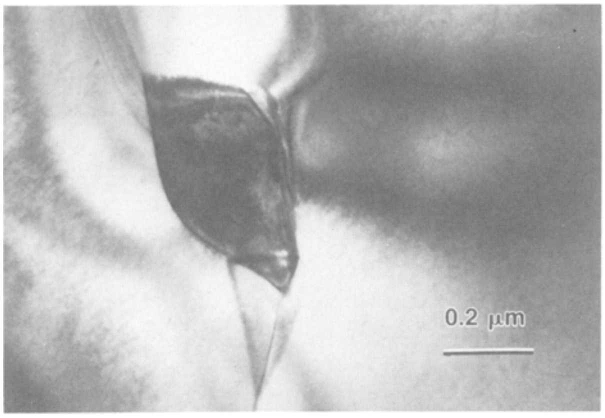

Figure 2 Transmission electron bright field micrograph of La_2O_3-rich grain boundary precipitate in 9 mol % La_2O_3–Y_2O_3 sample quenched after 1 min at 2100° C.

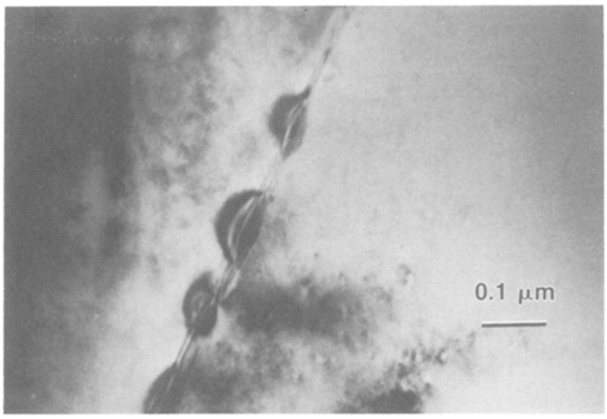

Figure 3 Transmission electron bright field micrograph exhibiting grain boundary strain contrast indicating the initial stages of precipitation in a 9 mol % La_2O_3–Y_2O_3 sample annealed 10 min at 2100° C.

of the lanthanum L peak (the element present in smaller amounts) was established and X-ray counting continued for each analysis point until 100 000 counts were obtained within the window region. This was done to minimize any errors due to poor counting statistics [18, 19].

Intensities for the yttrium L (I_Y) and lanthanum L (I_{La}) peaks were ratioed after performing a background subtraction. With the known concentrations of each element (C_Y and C_{La}) in the foil as obtained from wet chemistry analysis, the *k*-factor was then determined according to the familiar Cliff–Lorimer relation [19]

$$(C_Y/C_{La}) = k_{YLa}(I_Y/I_{La})$$

3. Results

3.1. *k*-factor determination

Chemical ICP analyses of the 9 mol % lanthana–yttria solid solution material used for the experimental determination of the *k*-factor for this system revealed lanthanum concentrations of 11.63 wt % and yttrium contents of 68.01 wt % for a total of 9.87 mol % La_2O_3.

k-factor measurements were performed in both the TEM and the STEM modes on thin foils prepared from the bulk. Measured values obtained after dividing observed X-ray intensity ratios of the two elements by their concentration ratios in the foil (as determined by wet chemistry) ranged from 0.54 to 0.58 for both TEM and STEM modes. The *k* values were then tested on the 9 mol % standard to determine which yielded compositions closest to that of the ICP analysis and that value was then employed. In this work all chemical analyses were performed in STEM mode using *k*-factor of 0.54 ± 0.02.

3.2. Precipitation studies

Microanalyses were performed on sintered 9 mol % lanthana–yttria specimens that were annealed in the two-phase field for various amounts of time before being quenched to room temperature.

Grain boundary precipitation predominates in samples annealed at 2100° C. After 1 min at this temperature, precipitates nucleate on the grain boundary as regularly shaped La_2O_3 rich particles approximately 1 μm in size (Fig. 2). Fig. 3, although not a typical micrograph for the sample annealed 10 min at 2100° C exhibits strain contrast on the grain boundary indicating the initial stages of the precipitation process. For anneals longer than 10 min the grain boundary phase appears as elongated structures (Fig. 4a). The backscattered electron microprobe image of the bulk sample annealed for 300 min shows the distribution of the second phase (Fig. 5).

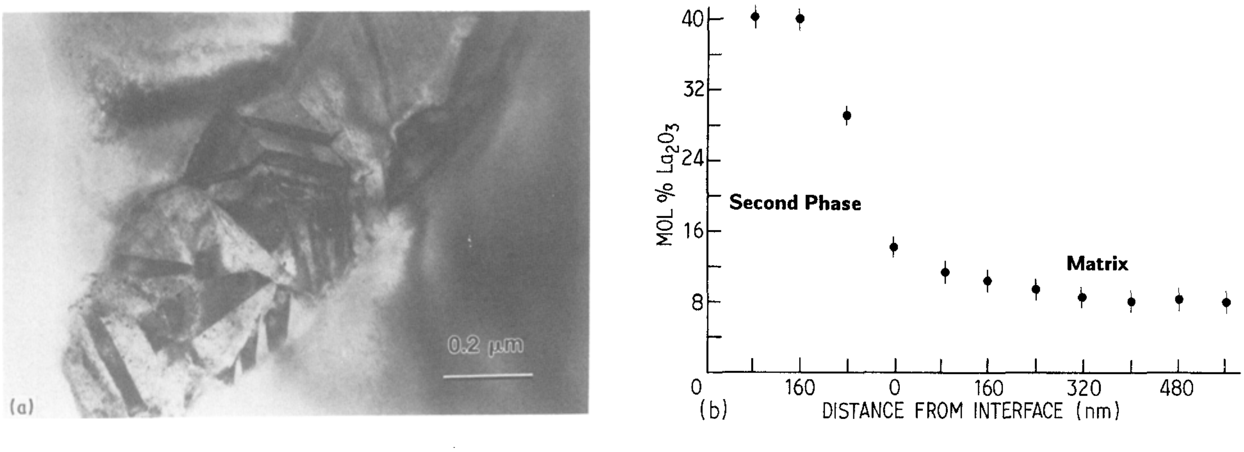

Figure 4 (a) Bright field micrograph of precipitate in sample annealed 300 min at 2100° C showing twin substructure. (b) The corresponding La_2O_3 concentration profile across the matrix–precipitate interface for the precipitate shown in (a).

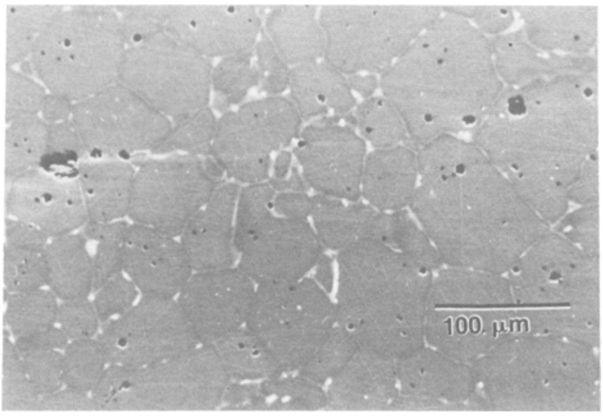

Figure 5 Backscattered electron micrograph of polished section of 9 mol % La_2O_3–Y_2O_3 sample annealed for 300 min at 2100° C showing the distribution of the second phase.

The second phases in the samples annealed for long times contain a substructure of twins and exhibit an overall facetted appearance. Strained interfaces can also be noted in the bright field images of Figs 4a and 6a between both the facetted regions or sections of the second phase as well as between the second phase itself and the matrix.

Scanning transmission electron microscopy (STEM) X-ray microanalyses were performed on the precipitate shown in Fig. 4a and the results are shown in Fig. 4b. The matrix exhibits concentrations of La_2O_3 in close agreement with the value depicted by the phase diagram (8–9 mol % lanthana). However, the second phase contains a lanthana content as high as 38 to 40 mol %, far in excess of that predicted by the cubic–hexagonal and hexagonal solvus (22–23 mol % lanthana). A similar analysis across the twinned second phase of Fig. 6a yields the same observations (Fig. 6b).

The samples annealed at 2200° C further into the two-phase field exhibit precipitation within the grain as well as on the grain boundary. The backscattered electron micrograph of the sample annealed 300 min at 2200° C shows the distribution of the second phase (Fig. 7). After 1 min at temperature the precipitates are seen to nucleate heterogeneously on dislocations as shown in Fig. 8. The bright field micrograph of Fig. 9a taken from the same sample exhibits a second phase of a grain like morphology. The associated diffraction pattern of Fig. 9b obtained from the untwinned region of the second-phase indexes as a $[\bar{2}\,\bar{1}\,1]$ zone of the hexagonal system. Thus this heat treatment appears to have successfully quenched in the hexagonal phase. After 10 min at 2200° C, the second phase begins to exhibit a rod-like appearance as shown in Fig. 10. Microstructures in samples annealed for 300 min consist almost exclusively of the long rod-like second phases (Fig. 11). Most of the second phases in these samples nucleate within the grain and show a preferred growth direction and orientation relationship with the cubic matrix.

Microdiffraction patterns of the elongated precipitates in the samples annealed for 300 min (Fig. 12a) reveal these second phases to be of monoclinic symmetry (Fig. 12b). Fig. 12c exhibits two overlapping selected area diffraction patterns from the cubic matrix and monoclinic second phase obtained by placing the selected area aperture around adjacent phases. This pattern indicates that the monoclinic structures orient themselves within the (body centred) cubic matrix such that the $(\bar{4}\,0\,2)_{\mathrm{monoclinic}}$ plane is approximately parallel to the $(\bar{2}\,2\,\bar{2})_{\mathrm{cubic}}$.

The STEM X-ray microanalysis profile (Fig. 13b) across the precipitate shown in Fig. 13a found in the sample annealed 300 min at 2200° C exhibits a La_2O_3 content in the matrix in agreement with phase diagram predictions (6–7 mol % lanthana) and a second phase La_2O_3 concentration near 25–26 mol %. Again the second-phase lanthana concentrations exceed phase diagram predictions (19 mol % lanthana at 2200° C). Analyses on other precipitates such as those shown in Fig. 14a yield similar results (Fig. 14b). All the needle-like precipitates exhibit composition invariance along the length of the precipitate as evidenced by the STEM analysis of Fig. 15.

4. Discussion

4.1. *k*-factor determination

During the course of the *k*-factor determination, some inconsistencies were observed in the intensity ratios obtained which resulted in erroneous *k*-factor measurements. X-ray counting was performed for each analysis point until a total of 100 000 counts were obtained in the smallest (La) peak. However at times wide

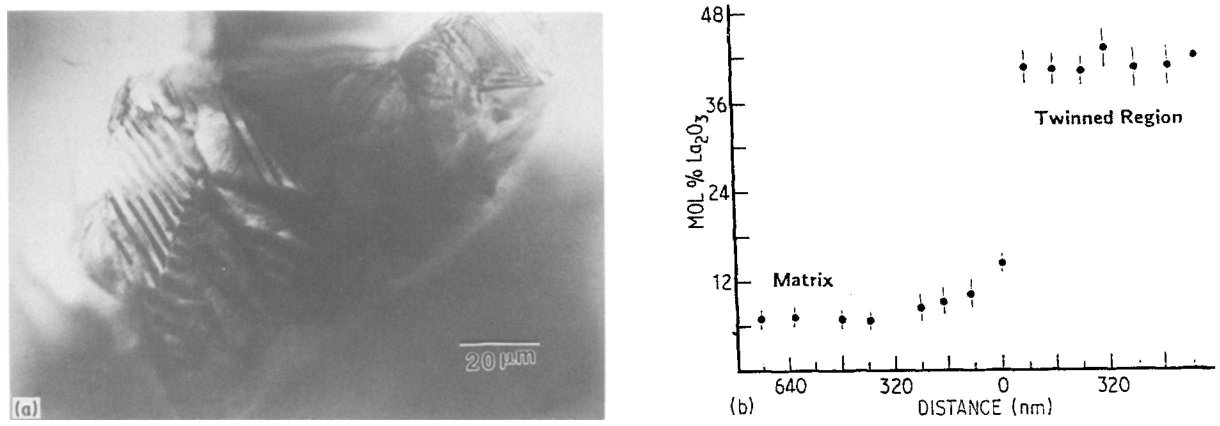

Figure 6 (a) Bright field micrograph of the second phase of a different morphology obtained in sample annealed for 300 min at 2100° C. (b) Corresponding microanalysis across interface separating matrix and the twinned region of the second phase shown in (a).

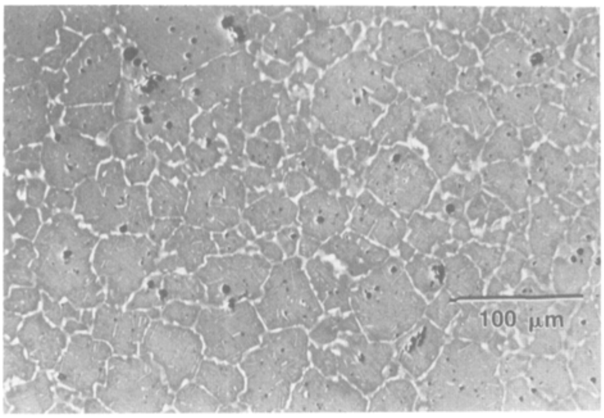

Figure 7 Backscattered electron micrograph of polished section from 9 mol % La_2O_3–Y_2O_3 sample annealed 300 min at 2200° C showing the distribution of the second phase.

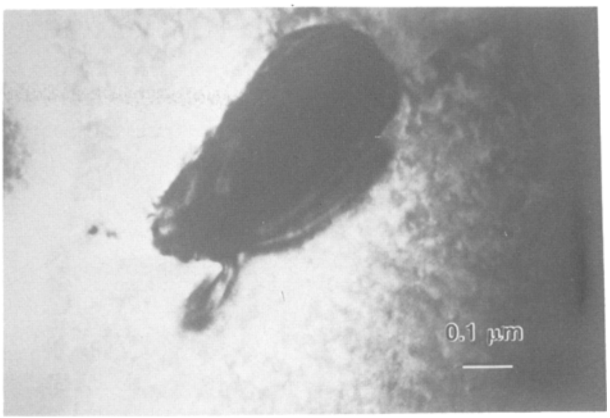

Figure 8 Transmission electron micrograph of second phase found in 9 mol % La_2O_3–Y_2O_3 sample annealed for 1 min at 2200° C.

variations of I_Y/I_{La} ratio occurred depending upon the thin foil and the area of analysis. These variations may be a direct result of (a) absorption by the sample, (b) electron beam damage to the foil or (c) contamination, and each of these possibilities was investigated.

For 9 mol % La_2O_3/Y_2O_3 samples, the thin film criterion limit indicates a critical thickness of approximately 200 nm beyond which a correction factor must be applied to the Cliff–Lorimer relation to account for absorption of X-rays by the sample [20]. The low energy yttrium L X-rays are the one most easily absorbed by the sample and in the isolated cases where the I_Y/I_{La} ratio was found to be considerably different than the average, it was always less than and never greater than the average indicating a yttrium deficiency. However STEM analyses were always performed on foil edges in thin regions of the sample using a spot size and second condenser lens aperture large enough to achieve a dead time of 20% or less. Thickness measurements obtained by convergent beam diffraction from some of the analysis areas revealed foil thicknesses below the critical limit. Therefore absorption by the sample was ruled out as a cause of inconsistent intensity ratios.

Electron beam damage to the foil was also studied since some elements are unstable under the electron beam and migrate during exposure due to the incident electrons. Lanthanum and yttrium are heavy elements and are unlikely to be affected by the beam, however, in an attempt to attain 100 000 counts in the lanthanum L peak the beam was held stationary on the same area for times that were as long as 80 min in some cases. In order to assess the sample stability as a function of counting time, counts were collected in a series of 100 sec intervals from a thin portion of the foil and the intensity data of both the yttrium and the lanthanum peaks were recorded after each interval. After 15 min, the ratioed intensities I_Y/I_{La} were plotted against the amount of time the beam was held stationary on the sample. Fig. 16 shows the linear fit to the data with zero slope indicating that for times as long as 15 min, no sample degradation was observed.

Silicon contamination was determined to be the reason for the anomalies observed in some of the data collected. At times, the amount of silicon was significant enough to result in a ring pattern superimposed on the selected area diffraction pattern obtained from a region of the foil on which the silicon lay. This contaminant appeared in the EDS display as well, but due to the relative energies of the peaks studied, its presence was not always easily recognized. The silicon K peak lies at the low energy end of the spectrum (1.84 keV), partially overlapping the yttrium L peak on its lower energy side. The yttrium L peak naturally exhibits a "tail" or a region of raised background on its lower energy side which diminishes with decreasing

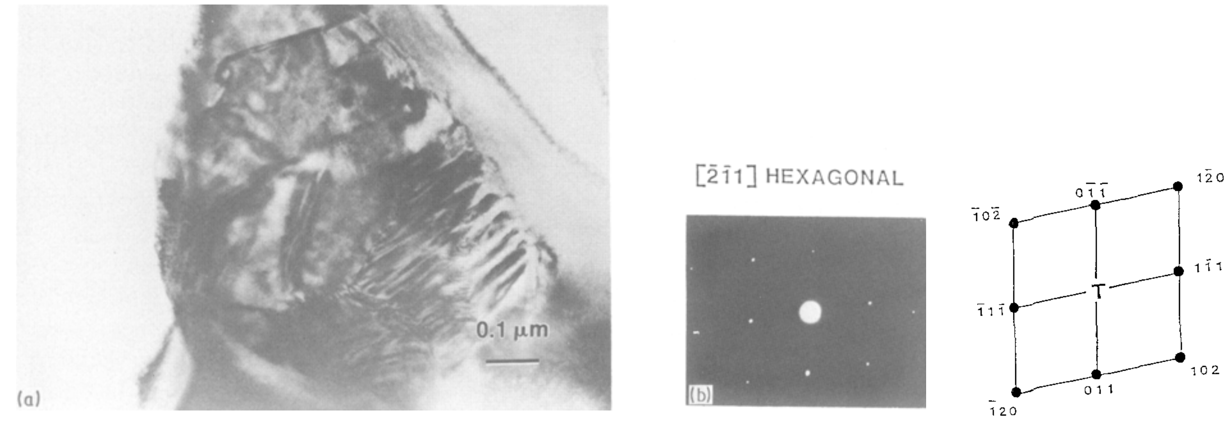

Figure 9 (a) Bright field micrograph of the second phase in 9 mol % La_2O_3–Y_2O_3 sample annealed for 1 min at 2200° C. (b) The corresponding diffraction pattern of the untwinned area in (a) showing hexagonal symmetry.

Figure 10 Transmission electron bright field micrograph of rod-like second phase exhibiting twin structures found after 10 min at 2200° C.

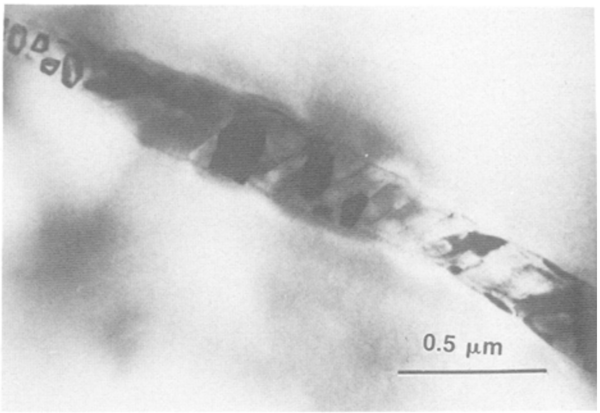

Figure 11 Typical microstructures obtained after 300 min at 2200° C showing elongated rod or lath-like morphologies.

energies from the yttrium L peak. The silicon K peak can be confused as part of this tail region, however in cases where the contamination becomes significant or when extended count times are used, the overlap of the silicon K and yttrium L peaks produces an extremely sharp shoulder on the low energy side of the yttrium peak which raises the background much above normal. This, in conjunction with silicon's large mass absorption coefficient for yttrium L X-rays ($\mu/\varrho = 3000$) [21] yields poor background fits of the data to the standard and erroneous intensity ratios.

Silicon contamination proves to be a serious threat to reliable quantitative analyses in the Y_2O_3/La_2O_3 system and in other yttria containing ceramics as well. The problem can be alleviated by utilizing the yttrium K peak in the quantitative analysis for which the silicon mass absorption coefficient is much lower ($\mu/\varrho = 11$) or by removal of the contaminant. In the present investigation, silicon contamination was traced to the ion beam thinner which operates with a silicon-based pump oil that vaporized and condensed on the sample when the sample remained idle in the thinner too long after the beams shut off. Successful removal of the silicon was performed simply by ion milling the sample a short time before immediately removing it from the thinner.

4.2. Precipitation studies

According to the phase diagram, 9 mol % La_2O_3-doped Y_2O_3 samples annealed at 2100° C lie close to the cubic–cubic and hexagonal phase boundary not very far into the two-phase region. As a result, the driving force for homogeneous nucleation in the grain is relatively weak and heterogeneous nucleation on the grain boundary can be expected. It is this heterogeneous boundary nucleation that is most likely responsible for grain boundary pinning during the transient second-phase sintering technique described earlier.

The second phase in the sample annealed for 300 min (Fig. 6a) exhibits a twinlike substructure and an overall facetted appearance. This was observed in nearly all precipitates studied in samples annealed for long times at either temperature and the microstructures resemble results obtained from TEM observations of the hexagonal to monoclinic phase transformation in other rare earth oxide systems [6–14].

According to the literature, the hexagonal and monoclinic polymorphs of the rare earth oxides are closely related layered structures of metal–oxygen tetrahedra stacked parallel to the basal plane of the hexagonal cell and to the $(2 0 \bar{1})$ plane of the monoclinic structure. Slight displacements of the hexagonal cell in three equivalent directions perpendicular to the *c* axis yield three variants or domains of the monoclinic phase. Boulesteix *et al.* and Yangui, Salem, and Dobie [7–14] have shown in other systems that these domains can grow as a result of interfacial strain. This strain induced driving force together with the observed twinning of the crystals along $\{3 1 3\}$ and $\{1 1 1\}$ planes of the monoclinic phase lends credence to a martensitic character to the hexagonal to monoclinic transformation.

In the present study, microdiffraction patterns of the elongated precipitates in the samples annealed for 300 min showed the second phases to be of monoclinic symmetry (Fig. 12b and 12c). The partitioned, strained nature of the second phase as depicted by Figs 4a and 6a may be a direct result of the hexagonal to monoclinic transformation, each section being one of the monoclinic domains observed to occur in other rare earth oxide systems.

Although micrographs obtained of the monoclinic phase in the yttria–lanthana binary do indicate similarities to the hexagonal to monoclinic transformation in other rare earth oxide systems the microanalyses of the second phases in the former indicate that the transition did not occur in a diffusionless manner. The absence of compositional invariance in the present case is a major difference observed in the yttria–lanthana system with respect to the same transformation in the other rare earth systems where the transition is believed to occur in a diffusionless, displacive, and possibly martensitic manner.

The microanalysis profiles also do not conform to typical nucleation and growth profiles. Typical nucleation and growth profiles usually exhibit a solute depletion zone adjacent to the interface which decreases with time to the equilibrium concentration. To observe the interface concentration microanalytically, the precipitate interface must extend through

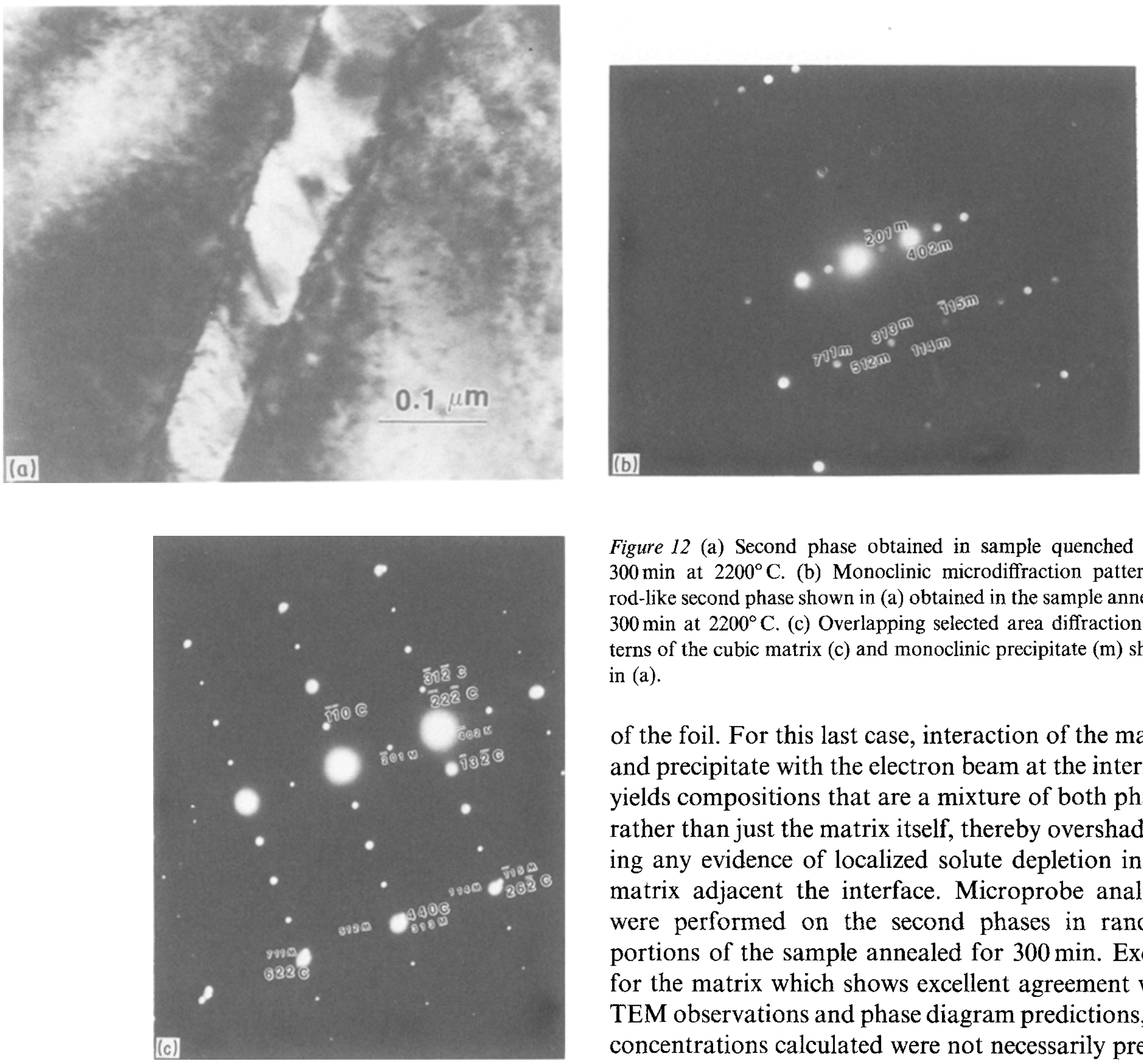

Figure 12 (a) Second phase obtained in sample quenched after 300 min at 2200° C. (b) Monoclinic microdiffraction pattern of rod-like second phase shown in (a) obtained in the sample annealed 300 min at 2200° C. (c) Overlapping selected area diffraction patterns of the cubic matrix (c) and monoclinic precipitate (m) shown in (a).

the thickness of the foil and it must be tilted parallel to the electron beam. In the samples annealed to 2100° C for 300 min, the La_2O_3 concentration increased from 8 or 9 mol % in the matrix to 12 to 16% near the interface to a final concentration of 38 to 40% in the second phase itself (Figs 4b and 6b). The absence of the depletion zone indicates that (a) the system has reached equilibrium, (b) the precipitate is dissolving, or (c) the facetted nature of the second phase is not yielding interfaces that extend through the thickness of the foil. For this last case, interaction of the matrix and precipitate with the electron beam at the interface yields compositions that are a mixture of both phases rather than just the matrix itself, thereby overshadowing any evidence of localized solute depletion in the matrix adjacent the interface. Microprobe analyses were performed on the second phases in random portions of the sample annealed for 300 min. Except for the matrix which shows excellent agreement with TEM observations and phase diagram predictions, the concentrations calculated were not necessarily precise since the size of the second phase was usually below the resolution limits of the instrument. Nevertheless a number of the second phase area samples yielded La_2O_3 concentrations as high as 37–38 mol %. Rhodes and coworkers also report similar findings of second-phase lanthana concentrations exceeding the cubic–hexagonal and hexagonal solvus [22].

The samples annealed at 2200° C (further into the two-phase field) exhibit precipitation within the grain typical of a higher driving force for nucleation. STEM analyses of the second phases obtained after long times at temperature exhibit La_2O_3 contents which rise

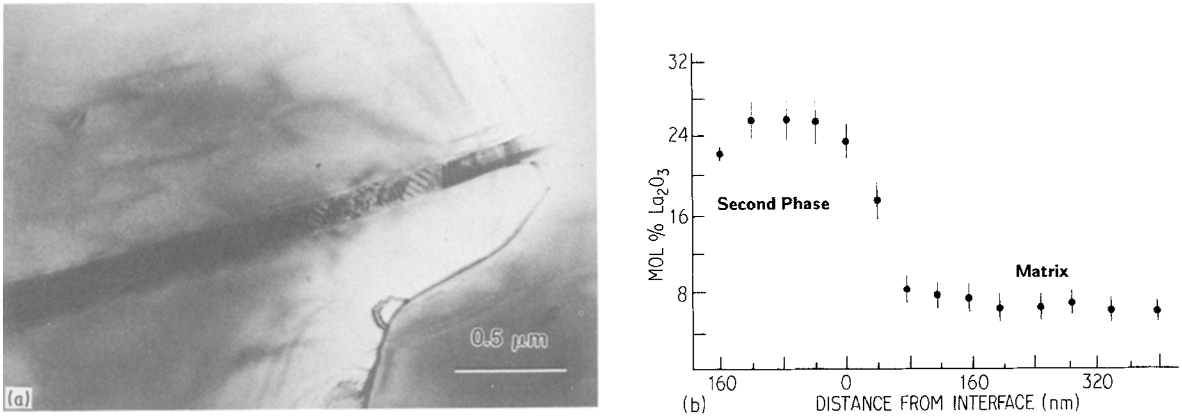

Figure 13 (a) Elongated precipitate found in sample annealed 300 min at 2200° C. (b) The microanalysis profile across the precipitate–matrix interface for the second phase shown in (a).

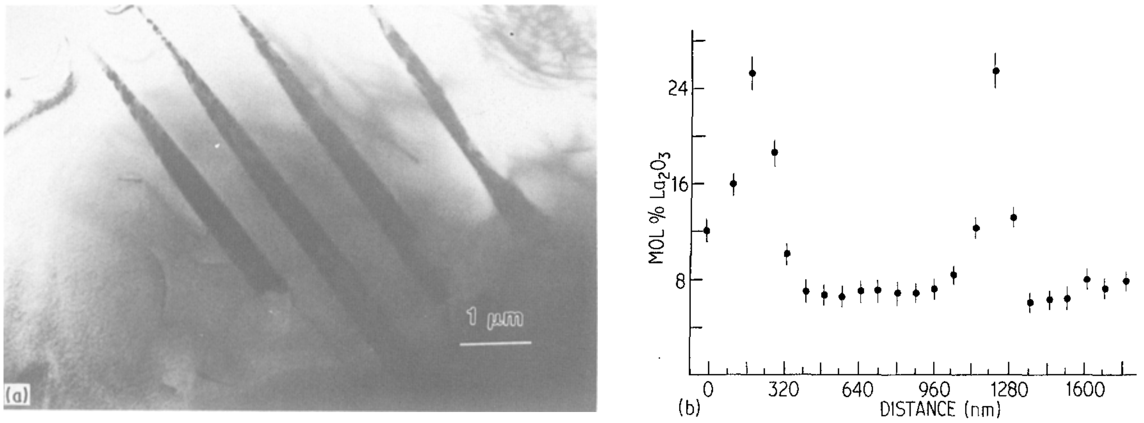

Figure 14 (a) Series of precipitates found after 300 min at 2200° C. (b) The microanalysis profile across two of the second phases of (a) showing the variation of the La_2O_3 content between precipitate and matrix.

from 6 to 7 mol % in the matrix to 16 to 18% near the interface to a final concentration of 24 to 27% in the second phase. The depletion zone is again absent and the profiles resemble dissolution profiles rather than nucleation and growth profiles. Again the second-phase concentrations of the samples annealed for 300 min exceed the limits defined by the hexagonal–cubic and hexagonal solvus boundary while the matrix concentrations agree very well with phase diagram predictions. All analyses were taken in precipitates lying on the edge of the foil and thickness estimations by the convergent beam diffraction technique on the samples revealed that the thin film criterion was upheld. Microprobe analyses confirmed the STEM microanalysis results as well.

The most likely cause of the discrepancy in the data results from re-equilibration of the phases at a lower temperature during the quenching procedure that perhaps was not severe enough to maintain the compositions of the equilibrium high temperature phases. Samples were quenched from the heat treating temperature by cutting the power to a tungsten mesh resistance heated furnace. Recorded temperature profiles indicated that the temperature dropped approximately 700° C in the first minute and a half. However, diffusion kinetics may have been fast enough to allow dissolution of the second phase or perhaps re-equilibration of the second phase at temperatures between 1400 to 1800° C. Self diffusion coefficients for polycrystalline yttrium oxide range from 10^{-10} to 10^{-9} $cm^2\,sec^{-1}$ for temperatures between 1400 and 1800° C as determined by Berard and Wilder [23]. No diffusion data was found on lanthana-doped yttria. However, due to cubic yttria's non-close packed defect fluorite structure whereby one quarter of the tetrahedral sites are void of an oxygen atom, it can be expected that diffusion in the yttria matrix is rapid enough to allow substantial compositional adjustment at the temperatures involved in this study if cooling rates are not fast enough.

The concentration profiles resemble dissolution profiles showing increasing amounts of La_2O_3 as the precipitate–matrix interface is approached and then reach a maximum in the second phase. However, the maximum is not the concentration dictated by the cubic–hexagonal and hexagonal solvus boundary at the heat treating temperature, but a value in excess of this.

Fig. 17 shows the two phase cubic and monoclinic region to extend from concentrations of La_2O_3 of approximately 15 to 40 mol %. According to the present STEM results, interface concentrations indicated approximately 16 mol % lanthana and precipitate contents of 38–40% for samples quenched from 2100° C. The cubic phase in this two-phase region contains lanthana contents of approximately 16 mol % similar to the interfacial concentrations. It is, therefore, believed that the second phase is transforming in such a manner that the cubic phase of the higher lanthana content (16 mol %) is nucleating at the interface of the matrix (cubic matrix of lower lanthana content approximately 8–9 mol %) and the precipitate.

The samples annealed at 2200° C yield interface

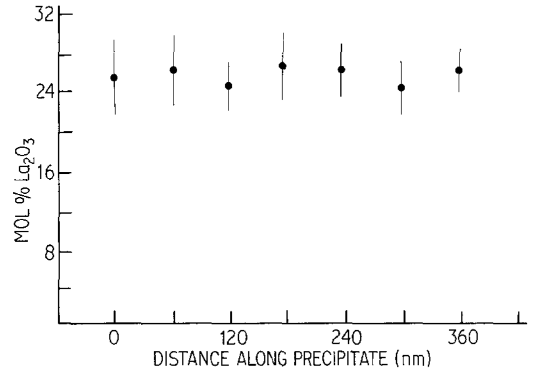

Figure 15 Microanalysis results along one of the precipitates of Fig. 14a showing composition invariance.

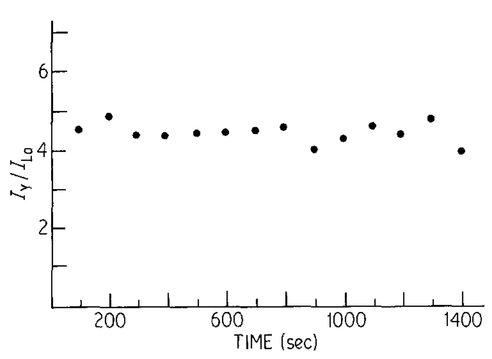

Figure 16 Plot of the ratio of the yttrium to lanthanum intensities against time of exposure to electron beam.

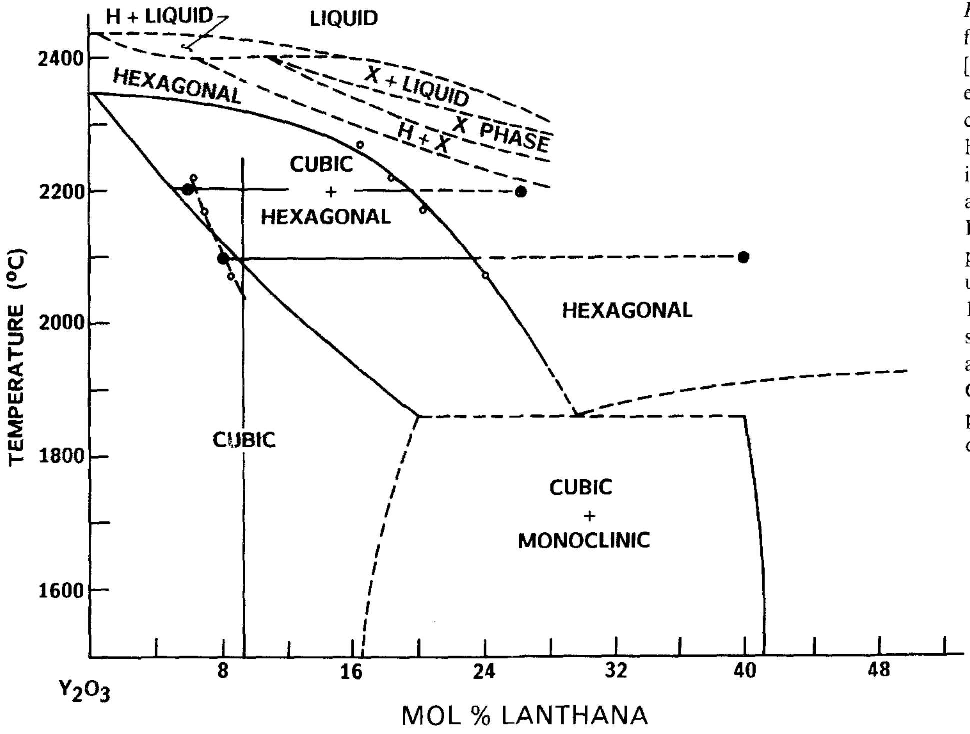

Figure 17 Phase diagram taken from combined results of Mizuno [16] and Coutures and Foex [17] exhibiting limits for solubility of cubic and monoclinic region at high temperatures. Open circles in the cubic and hexagonal region are data points obtained by Rhodes and coworkers by microprobe analyses on large individual abnormal grains of a 12 to 14 mol % La_2O_3-doped Y_2O_3 sample sintered at 2070 to 2270° C and quenched to 1400° C in 1 min. Closed circles represent results of present study on 9 mol % La_2O_3-doped Y_2O_3 specimens.

concentrations compatible with the cubic and cubic–monoclinic solvus but second-phase concentrations that comply with neither the cubic–hexagonal and hexagonal nor the cubic–monoclinic and monoclinic solvus, possibly indicating that the equilibration has not gone to completion.

5. Conclusions

Microstructures obtained in 9 mol % lanthana doped yttria samples quenched after long time anneals at 2100° C just inside the cubic–cubic and hexagonal solvus exhibit predominantly intergranular precipitates of monoclinic symmetry, containing a facetted substructure of twins. Samples annealed for the same times at 2200° C (further into the two-phase field) exhibit both intergranular and intragranular precipitation, the dominant morphology being long rod-like precipitates containing a substructure and exhibiting a preferred orientation in the matrix.

Microchemical analyses were performed on the samples given long time anneals at 2100 and 2200° C. This required measurement of the *k*-factor for this system. During the course of the *k*-factor analysis, it was found that silicon contamination from silicon based pump oils used in the ion beam thinner imposes gross absorption of yttrium L X-rays and EDS artifacts that result in poor background fits when using yttrium L lines in quantitative analyses. When the problem was corrected, chemical microanalyses on the microstructures obtained in samples annealed 5 h at temperature revealed equilibrium matrix concentrations and second-phase concentrations far in excess of that predicted by the cubic–hexagonal and hexagonal solvus. The most likely cause of the discrepancy is a transformation of the hexagonal phase during the quench from the cubic and hexagonal field and an attempted equilibration in the two-phase cubic and monoclinic region.

Acknowledgements

The authors would like to thank Dr W. H. Rhodes and Dr G. C. Wei of GTE Laboratories, Waltham, Massachusetts for supplying the samples used in this study as well as for the many helpful discussions conducted throughout the course of this research. The financial support provided by the United States Department of Energy through grant No. DE-FG02-84ER45150, is also gratefully acknowledged.

References

1. W. H. RHODES, *J. Amer. Ceram. Soc.* **64** (1981) 13.
2. C. GRESKOVICH and I. P. CHERNOCH *J. Appl. Phys.* **44** (1973) 4599.
3. K. A. WICKERSHEIM and R. A. LEFEVER, *J. Opt. Soc. Am.* **51** (1961) 1147.
4. P. J. JORGENSEN and R. C. ANDERSON, *J. Amer. Ceram. Soc.* **50** (1967) 553.
5. G. C. WEI, T. EMMA, W. H. RHODES, S. HORVATH and M. P. HARMER, *J. Amer. Ceram. Soc.* **71**[10] (1988) 820.
6. P. E. CARO, *J. Less Common Met.* **16** (1968) 367.
7. P. C. BOULESTEIX, P. CARO, M. GASGNIER, Ch. H. LABLANCHETAIS and G. SCHIFFMACHER, *Acta Crystallogr. A*, **27** (1971) 552.
8. P. C. BOULESTEIX, B. PARDO, P. CARO, M. GASGNIER and Ch. H. LABLANCHETAIS, *Acta Crystallogr. B*, **27** (1971) 216.
9. P. C. BOULESTEIX, P. CARO, M. GASGNIER, Ch. H. LABLANCHETAIS and G. SCHIFFMACHER, *Phys. Lett.* **34A** (1971) 437.
10. M. B. SALEM, R. DOBIE and B. YANGUI, *Phil. Mag. A* **50** (1984) 621.
11. P. E. CARO, G. SCHIFFMACHER, C. BOULESTEIX, Ch. LOIER and R. PORTIER, in "Defects and Transport in Oxides", edited by S. Seltzer and R. I. Jaffee (Plenum Press, New York, 1974) p. 519.
12. C. BOULESTEIX, B. PARDO, L. VALIERGUE, P. CARO, M. GASGNIER and Ch. H. LABLANCHETAIS, *Phys. Lett.* **32A** (1970) 361.
13. C. BOULESTEIX and B. YANGUI, *Phys. Status Solidi* **70** (1982) 597.
14. *Idem., ibid.* **73** (1982) 515.

15. G. C. WEI, GTE Laboratories, private communication (1984).
16. M. MIZUNO, A. ROUANET, T. YAMADA and T. NOGUCHI, *Yogyo Kyokai Shi*, **84** (1976) 342.
17. J. COUTOURES and M. FOEX, *J. Solid State Chem.* **11** (1974) 294.
18. J. I. GOLDSTEIN J. L. COSTLEY, G. W. LORIMER and S. J. B. REED, *Scanning Electron Microsc.* **I** (1977) 315.
19. D. B. WILLIAMS, in "Practical Analytical Electron Microscopy in Materials Science" (Philips Electron Optics Publishing Group, Mahwah, NJ, 19) Ch. 4.
20. B. A. BENDER, D. B. WILLIAMS and M. R. NOTIS, *J. Amer. Ceram. Soc.* **63** (1980) 149.
21. K. F. J. HEINRICH, "The Electron Microprobe", edited by T. D. McKinley, K. F. J. Heinrich, and D. B. Wittry (John Wiley, New York, 1966) p. 296.
22. G. C. WEI, GTE Laboratories, Private communication (1985).
23. M. F. BERARD and D. R. WILDER, *J. Appl. Phys.* **34** (1983) 2318.

Received 8 January
and accepted 9 May 1988